Biophysical Journal

# Spectral Analysis Methods for the Robust Measurement of the Flexural Rigidity of Biopolymers

David Valdman*, Paul J. Atzberger*‡, Dezhi Yu†, and Megan T. Valentine‡

*Department of Mathematics, †Department of Materials, ‡Department of Mechanical Engineering, University of California, Santa Barbara CA 93117, USA

ABSTRACT The mechanical properties of biopolymers can be determined from a statistical analysis of the ensemble of shapes they exhibit when subjected to thermal forces. In practice, extracting information from fluorescent microscopy images can be challenging due to low signal-to-noise ratios and other artifacts. To address these issues, we develop a suite of robust tools for image processing and spectral data analysis. These are validated through a systematic benchmarking approach to assess robustness and accuracy. Our methods are based on a biopolymer contour representation expressed in a spectral basis of orthogonal polynomials. We extract information about the biopolymer using global fitting routines that optimize a utility function measuring the amount of fluorescence intensity overlapped by such contours. This approach allows for filtering of high-frequency noise and interpolation over sporadic gaps in fluorescence. To demonstrate the validity of our methods, we analyze an ensemble of simulated images, having realistic types of noise and artifacts, which is generated from the fluctuations of a simulated biopolymer with known stiffness. To demonstrate our methods in practice, we perform analysis of experiments of fluctuating microtubules. Overall, we expect these new approaches to be useful in the study of biopolymer mechanics and the effects of associated regulatory molecules.

Last update to manuscript PDF was on June 27, 2011; 3:15pm.

Address reprint requests and inquiries to P.J. Atzberger with e-mail: atzberg@math.ucsb.edu.

## 1. INTRODUCTION AND BACKGROUND

Cytoskeletal polymers, including actin and microtubules, are stiff, multi-stranded filaments that are essential to cell organization, motility, and division; to the transport of intracellular cargos by motor proteins; and to the generation and transmission of forces within and across cells. Because of their important role in establishing and regulating cellular mechanics, the elasticity of filaments and entangled cytoskeletal networks has been studied extensively. However, many important questions remain about the relationships between structure and mechanics [1].

In particular, although *in vitro* measurements of single filament elasticity have consistently shown significant variations in stiffness over roughly an order of magnitude, the molecular origins of these variations are incompletely understood [2, 3, 4, 5, 6, 7]. This is largely a result of an inability to distinguish real heterogeneity in elasticity from variations that arise from sources of experimental and statistical uncertainty. For microtubules (MTs), the stiffest cytoskeletal filaments, distinguishing between signals and noise is particularly challenging since the exhibited bending amplitudes are small and often of a comparable magnitude to experimental noise.

Microtubules play essential and diverse roles in cellular systems, and inherent mechanical variations in microtubule stiffness may play an influential part in processes regulating cellular behavior [8, 9, 10, 11, 12]. Microtubules are formed from the head-to-tail polymerization of tubulin dimers in long protofilaments that interact laterally to form a closed tubular structure [13, 14, 15, 16]. In general, the lattice formed by the lateral association of dimers has a continuous dislocation called a seam, the mechanical implications of which are not fully understood [17]. Structural studies have demonstrated that the number of MT protofilaments varies within *in vitro* and *in vivo* systems, and can even change along the length of a single MT [18, 19, 20]. According to elastic beam theory, the bending stiffness of a biopolymer scales as the fourth power of its radius. This suggests that even small changes in the effective radius of the microtubule could have a large mechanical effect.

For *in vitro* systems, MT stiffnesses also appear to depend on both the length and the polymerization velocity, suggesting that lattice shear and structural defects may play an important role [5, 21, 22, 23]. Other studies have shown that the binding of microtubule associated proteins (MAPs) can influence the stiffness of the composite material [4, 6]. MAP proteins play an important role in many cellular processes, such as neurogenesis, axonal transport, and mitosis, and a number of MAP-specific mutations have been linked to human diseases [10, 24, 25, 26].

Unfortunately, the large variation in experimental estimates of MT stiffness values has severely compromised our ability to compare various polymerization conditions or the differential effects of the various classes and isoforms of essential MAPs. This has prevented correlation between changes in mechanical response and filament composition, and has led to an incomplete understanding of how microtubule mechanics are regulated in cellular systems.

To help address these issues, we have developed new

methods to determine and analyze the motions of thermally fluctuating biopolymers visualized using fluorescence microscopy. Using approaches from statistical mechanics, we then infer mechanical properties from a spectral analysis of the ensemble of biopolymer configurations at thermal equilibrium. A central challenge in estimating mechanical properties using this approach is the sensitivity of the spectral analysis methods to experimental noise [4, 27]. Existing methods require (i) determination of the biopolymer configurations from the fluorescence images, (ii) calculation of spectral components from the inferred biopolymer configurations, and (iii) analysis of the spectral components using statistical mechanics to ascertain mechanical properties [4, 27, 5].

In this work, we develop new methods for spectral analysis that combine steps (i) and (ii) above into a single procedure, thus minimizing the introduction of errors. This is achieved by representing the biopolymer shape in terms of a contour expanded in an orthogonal polynomial basis. We use this representation to fit the coefficients of the expansion directly to the fluorescence image by optimizing a utility function that measures the overlap of the contour with fluorescence intensity. Our new methods allow for the robust determination of biopolymer shape even in the presence of significant noise and artifacts in the images. To estimate the flexural rigidity of the biopolymer, we develop a statistical mechanics theory based on an energy formulated directly in terms of the coefficients of our spectral biopolymer representation.

Our approach has a number of distinct advantages over previous methods. The description of the biopolymer by a smooth contour that is fit to the entire image at once naturally handles sporatic gaps in fluorescent intensity along the biopolymer through interpolation. Additionally, we achieve a more accurate description of the biopolymer near the endpoints. This is in contrast to a trigonometric Fourier basis that implicitly requires a periodic function to avoid spurious oscillations arising from Gibb's Phenomena [28]. In practice, a no curvature condition has often been imposed at the endpoints of the contour to avoid this effect [4, 27]; however, this can result in inaccuracies when estimating the effective flexural rigidity. Our methods are based instead on orthogonal polynomials and can in principle allow for curvature near the end-points, and could potentially facilitate studies of a wider class of biopolymers.

To assess the sensitivity of proposed methods for image and spectral analysis to experimental noise and sampling error, we introduce a benchmarking approach in which an ensemble of simulated images is generated from simulations of a fluctuating biopolymer with known mechanical properties. We introduce noise and artifacts into the images that are similar to those observed in experimental data sets. This approach allows for the systematic study of the roles played by different types of experimental noise, and the resultant uncertainty of estimated mechanical properties. The benchmarking approach we propose provides a potentially powerful metric for rating different spectral analysis methods and for understanding the statistical significance of differences reported in experimental results. We then apply the techniques to an experimental data set of fluorescence images taken of a fluctuating microtubule. For even these stiff biopolymers, we find our methods reliably estimate the flexural rigidity and produce modal covariances in agreement with a worm-like-chain model for the microtubule mechanics. We anticipate that these new approaches will facilitate the development of more sensitive assays based on the thermal fluctuations of biopolymers, and will enable central questions concerning the molecular origins of cytoskeletal mechanics to be answered.

## 2. METHODOLOGY

### 2.1 *Overview*

The success of our spectral analysis approach hinges on our ability to accurately determine the shapes exhibited by a thermally fluctuating biopolymer within a collection of fluorescence microscopy images. This shape determination can be challenging in practice, due to artifacts in the biopolymer signal resulting from non-uniform binding of dye molecules or photobleaching, as well as camera noise. This can present difficulties in generating a sufficient number of good quality images to ensure small statistical sampling errors. Therefore, improvements in the tolerance of fitting methods to allow for a larger number of images to be used could have important consequences for the quality of experimental results.

Previous methods to characterize the fluctuation spectra of biopolymer filaments make use primarily of local information in the fluorescent image. For example, contour paths have been obtained by interpolating individual configuration points that are determined by manual selection or by local fitting of the cross-sectional intensity profiles of fluorescently-labeled filaments [27, 4, 5]. However, since each control node is fit independently, any local aberration in the image near a control point could have a large influence on the entire fitted contour. Such local artifacts can come from a variety of experimental sources, such as irregularity in fluorophore labeling, the interference of a nearby physical object, and background noise. Though these approaches have been successfully employed to provide important mechanical information for many types of biopolymers, for the stiffest biopolymers, like microtubules, results vary by roughly an order of magnitude [29, 30]. These limitations indicate a clear need for further development of fitting methods.

To address these issues, we introduce new methods based on a variational approach that fits an entire contour at once to the fluorescence image. This global approach is more robust to small local disturbances in the fluorescence signal and to sporadic gaps in intensity along the biopolymer. We perform

the fit by starting with a trial contour for the biopolymer filament that is successively refined to minimize a utility function that measures the overlap of the contour with the fluorescence intensities of the image. To do this in practice a biopolymer is represented by coefficients for a contour expanded in a basis of orthogonal polynomials.

This representation provides for a unified approach where the coefficients used in the spectral analysis are directly obtained by fitting to the fluorescence image. This is in contrast to previous methods where the filtering of image background noise, the interpolation between control nodes, and the spectral analysis were all treated algorithmically as separate components. Our more unified approach results in methods exhibiting enhanced robustness when estimating mechanical properties.

### 2.2 *Variational Contour Fitting Method*

The biopolymer shape is described by a curve $\mathbf{x}(s)$ of length $L$, where $s \in [0, L]$ is the arc-length parameter of the contour. To measure how well the contour $\mathbf{x}$ overlaps with the fluorescence signal of the biopolymer we use the utility function

$$U[\mathbf{x}, I] = -\int_0^L \int_\Omega k(|\mathbf{y} - \mathbf{x}(s)|) I(\mathbf{y}) d\mathbf{y} ds. \qquad (1)$$

The fluorescent image intensity is given by $I = I(\mathbf{y})$ parameterized over the spatial domain $\Omega$ and $k(r)$ is a smoothing kernel vanishing for $r > r_0$.

The inner-integral of equation 1 gives the average intensity in a region near the location $\mathbf{x}(s)$ by using the weighting specified by $k(r)$. The outer-integral collects these values to provide a measure of the total amount of overlap of a contour with the biopolymer fluorescence signal. The convolution by $k(r)$ with $I$ filters the high spatial-frequency noise inherent in the image intensity.

We use the following kernel function (see Figure 1.)

$$k(r) = \begin{cases} \alpha[1 + \cos(\pi r / r_0)] & r \leqslant r_0 \\ 0 & r > r_0. \end{cases} \qquad (2)$$

Here, $r_0$ is chosen to be approximately equal to the width of the imaged polymer. In the case of microtubules, with a diameter of approximately 25 nm, $r_0$ is taken to be approximately equal to the the width of the point spread function of the microscope.

The $\alpha$ is a normalization constant ensuring the kernel function weighting integrates to one. This kernel can be shown to have a number of desirable properties when used for discrete pixel maps and lattice models, see [31, 32].

The contour configuration that minimizes the utility function $U$ provides a fit that maximizes the overlap within the image between the contour and the biopolymer fluorescence signal. To minimize the utility function in practice we require a representation for the contour amenable to calculations. For this purpose, we represent the contour by its tangent angle $\theta(s)$ along the length and by a reference point at the left end-point $\mathbf{x}_0 = \mathbf{x}(0)$. These physically meaningful degrees of freedom uniquely specify the contour curve $\mathbf{x}(s)$, which can be recovered by

$$\mathbf{x}(s) = \int_0^s \boldsymbol{\tau}(\theta(s'))ds' + \mathbf{x}_0. \qquad (3)$$

The tangent vector $\boldsymbol{\tau}$ for a given angle $\theta$ is given by $\boldsymbol{\tau}(\theta) = (\cos(\theta), \sin(\theta))$.

This representation is used to minimize the utility function by evolving the degrees of freedom $(\theta(s), \mathbf{x}_0)$ using the steepest descent dynamical equations

$$\begin{aligned} \frac{\partial \theta(s)}{\partial t} &= -\frac{\delta U}{\delta \theta}(s) \\ \frac{\partial \mathbf{x}_0}{\partial t} &= -\nabla_{\mathbf{x}_0} U. \end{aligned} \qquad (4)$$

The term $\delta U / \delta \theta$ denotes the variational derivative of the utility function. This term generalizes the usual vector derivative and captures how values change when the entire collection of tangent vectors along the contour are varied [33]. The $\nabla_{\mathbf{x}_0} U$ denotes the usual vector derivative in $\mathbf{x}_0$ of the utility function. This term captures how values change when the left end-point $\mathbf{x}_0$ is varied.

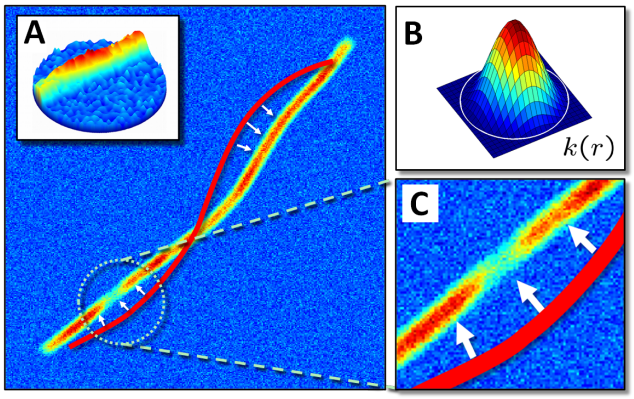


**FIGURE 1 Schematic of the Methodology: (A) The intensity of the fluorescence signal of the biopolymer (inset) and the fluorescence microscopy image being fit by a trial contour (red line). The white arrows indicate the direction of evolution of the trial contour when using the method of steepest descent for the utility function given in equation 1. (B) The radially symmetric kernel function $k(r)$ having cut-off radius $r_0$ (indicated by white dotted circle). (C) Close-up of fluorescent image data within the range of influence given by $r_0$. In this case, the fluorescence image exhibits gaps in intensity along the biopolymer that is handled naturally by the utility function and the inherent interpolation of the trial contour.**

It can be shown that for all possible variations of $(\theta(s), \mathbf{x}_0)$, the direction in configuration space giving the most rapid decrease in the utility function $U$ is the negative

of the gradient $-\nabla_{\theta(s),\mathbf{x}_0} U = -(\delta U/\delta\theta, \nabla_{\mathbf{x}_0} U)$. This motivates the choice for the dynamics, which ensures the contour configuration moves in a manner that steadily decreases the value of $U$ over time. The limiting contour configuration that is stationary under these dynamics has a zero gradient and is a critical point of the utility function $U$. Such a contour is a candidate for minimizing $U$ [33].

To work with this description in practice we expand the tangent angles in an orthogonal polynomial basis

$$\theta(s) = \sum_n a_n T_n(s). \tag{5}$$

Each $T_n(s)$ is a polynomial of degree $n$ satisfying the orthonormal inner-product condition $\langle T_i, T_j \rangle = \delta_{ij}$, where $\delta_{ij}$ is the Kronecker delta-function Figure 2. In practice, this expansion is truncated after a finite number of terms summing up only to degree $N$ polynomials. Dynamical equations are obtained readily for the coefficients $a_n(t)$ by plugging this expansion into equation 4 and projecting the direction of evolution on the polynomials up to degree $N$, see the Supplemental Materials.

A particularly useful feature of this coefficient representation is that even when only a finite number of coefficients are used the contour recovered by equation 5 and equation 3 has total arc-length $L$ throughout the minimization procedure. In presenting our approach, we use throughout the Chebychev orthogonal polynomials defined by $T_n(s) = \cos(n \arccos((2s/L) - 1))$, see [28]. This choice was motivated by the ability to take advantage of Fast Fourier Transform methods. However, after developing our methods this benefit was found to be modest. Other types of orthogonal polynomial bases could also be used, such as the Legendre polynomials orthogonal with the $L^2$-inner-product, which might provide some advantages when performing the spectral analysis. For more details concerning the particular forms of the variational derivatives used and truncation of the dynamics for a finite number of coefficients, see the Supplemental Materials.

### 2.3 *Determining Persistence Length from the Spectrum of Biopolymer Fluctuations*

Using results from equilibrium statistical mechanics, we can estimate the elastic properties of isolated, thermally fluctuating biopolymers [4]. We focus here on determining the persistence length; however, these methods can be applied more generally to other mechanical moduli.

To describe the elastic responses of biopolymers, we use the worm-like chain (WLC) model [34], which associates to a given biopolymer configuration $\mathbf{x}(s)$ a bending energy

$$E_{bend}[\mathbf{x}] = \frac{EI}{2} \int_0^L \left(\dot{\theta}(s)\right)^2 ds. \tag{6}$$

The $EI$ denotes the flexural rigidity and $\dot{\theta}(s) = d\theta/ds$ denotes the derivative of the tangent angle in $s$. For an isotropic elastic structure, $EI$ is the product of the Young's modulus $E$ and the geometric moment of inertia $I$, corresponding to the cross section of the biopolymer. At thermodynamic equilibrium, the biopolymer thermal fluctuations have a Gibbs-Boltzmann distribution with the probability density

$$\rho_{bend}[\mathbf{x}] = \frac{1}{Z} \exp[-E_{bend}[\mathbf{x}]/k_B T] \tag{7}$$

where $T$ is the temperature, $k_B$ is the Boltzmann constant, and $Z$ denotes the partition function, see [35].

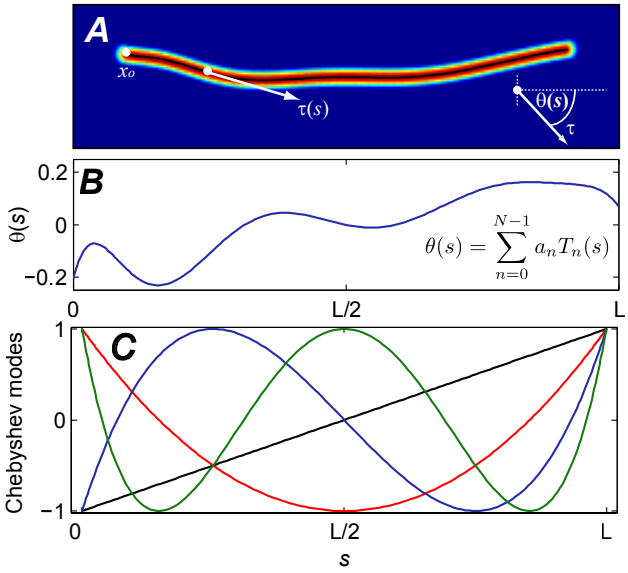


**FIGURE 2 Representation of the Biopolymer Shape using Orthogonal Polynomials : (A) The contour tracing out the shape of the biopolymer is described by parameterizing the shape using arc-length $s$ and giving the local angle $\theta(s)$ of the tangent vector $\tau$ with respect to the x-axis. The point $\mathbf{x}_0$ is used to uniquely determine the position of the contour. (B) To work with this description in practice we expand $\theta(s)$ in an orthogonal polynomial basis to obtain coefficients $a_n$. (C) We use the Chebychev orthogonal polynomial basis for this purpose. The first four non-constant orthogonal polynomial modes are shown.**

Using our representation of the biopolymer configuration $\mathbf{x}(s)$ in terms of coefficients of the orthogonal polynomial expansion (see equation 5), the energy can be expressed as

$$\begin{aligned} E_{bend}[\mathbf{a}] &= \frac{EI}{2} \mathbf{a}^T S \mathbf{a} \\ S_{ij} &= \int_0^L \dot{T}_i(s) \dot{T}_j(s) ds. \end{aligned} \tag{8}$$

The term $\mathbf{a}$ denotes the composite vector of coefficients with $[\mathbf{a}]_n = a_n$ and $S$ denotes the stiffness matrix of the biopolymer modes. We remark that the entries $S_{i,j}$ of the stiffness matrix are given by the $L^2$-inner product of the orthogonal polynomials with index $i$ and $j$, so the matrix is not necessarily diagonal. For example, for our choice of Chebyshev polynomials the off-diagonal entries of $S$ are non-zero, while for

other choices of polynomial bases, the matrix can be made strictly diagonal [28].

The Gibbs-Boltzmann distribution can be expressed using this coefficient representation as

$$\rho_{bend}[\mathbf{a}] = \frac{1}{\tilde{Z}} \exp\left[-\frac{1}{2} L_p \mathbf{a}^T S \mathbf{a}\right] \tag{9}$$

where $L_p = EI/k_BT$ gives the persistence length of the correlations of fluctuations along the contour and $\tilde{Z}$ is the partition function of this representation. In this form, we see that $\rho_{bend}$ has the convenient form of a multivariate Gaussian with mean zero and covariance

$$\langle \mathbf{a}\mathbf{a}^T \rangle = \frac{1}{L_p} S^{-1}. \tag{10}$$

In our analysis, we find it convenient for finite contours to define a non-dimensional persistence length. In particular, we define the relative persistence length by $\ell_p = L_p/L$. This gives the ratio of the persistence length $L_p$ to the total contour length $L$. The covariance structure for biopolymer fluctuations derived from the WLC model and equation 10 is given by

$$C_{\text{wlc}}(\ell_p) = \frac{1}{\ell_p} \tilde{S}^{-1}. \tag{11}$$

We have used the non-dimensional WLC stiffness matrix defined by $\tilde{S} = LS$. This provides a covariance structure predicted by the WLC model when the non-dimensional persistence length is $\ell_p$.

In experiments, the covariance is estimated by fitting contours to the fluorescence images and estimating modal coefficients. For $M$ samples, the covariance is estimated by

$$C_{\text{exp}} = \frac{1}{M} \sum_m \mathbf{a}^{(m)} \mathbf{a}^{(m)T}. \tag{12}$$

The $\mathbf{a}^{(m)}$ denotes the $m^{th}$ sampled modal coefficient.

A central relation we shall use to interpret experimental fluctuations of a biopolymer and to infer its mechanical properties is the following

$$C_{\text{exp}} = C_{\text{wlc}}(\ell_p). \tag{13}$$

This expression provides the key link between observed biopolymer fluctuations (left-hand-side) and the biopolymer mechanical properties (right-hand-side). To infer mechanical properties in experiments, we seek to find a value of $\ell_p$ so that $C_{\text{wlc}}$ matches to a good approximation the covariance of the experimentally observed biopolymer fluctuations $C_{\text{exp}}$.

This requires minimizing the least-squares error given by

$$V(\ell_p) = \sum_n \left(c_n - \frac{1}{\ell_p} d_n\right)^2. \tag{14}$$

We find in practice that it is sufficient to consider just the diagonal entries of the covariance matrix, thus the $c_n = [C_{\text{exp}}]_{n,n}$ are the diagonal entries of the covariance matrix for the experimentally observed biopolymer fluctuations. The $d_n = [\tilde{S}^{-1}]_{n,n}$ are the coefficients used for representing the covariances obtained from the WLC model, see equation 11. The fit for $\ell_p$ is obtained by minimizing $V(\ell_p)$ and is given by

$$\ell_p = \|\mathbf{d}\|^2/(\mathbf{d}\cdot\mathbf{c}). \tag{15}$$

We use composite vector notation for the experimental covariance data $[\mathbf{c}]_n = c_n$ and for the coefficients of the WLC model $[\mathbf{d}]_n = d_n$. The $\|\mathbf{d}\|^2 = \sum_n d_n^2$ and $\mathbf{d}\cdot\mathbf{c} = \sum_n c_n d_n$.

## 3. RESULTS AND DISCUSSION

### 3.1 *Robustness and Accuracy of Spectral Analysis Methods*

A prevalent issue in the field of force spectroscopy is the limited tools researchers have to assess whether the mechanical properties derived from spectral analysis are reliable and whether deviations from theoretical predictions reflect real physical features of a biopolymer, or are simply due to noise in the data. There are two fundamentally independent sources of error to consider. The first is the inherent problem of sampling error, where the derivation of mechanical quantities leads to errors due to an averaging over a finite number of experimental observations. The second is the effect of different types of noise in the microscopy images on the estimated values of physical quantities.

To investigate sampling error, we provide a theoretical treatment that describes how errors scale for a given number of experimental fluorescence images. To investigate the finer details of image noise and its consequences, we also develop a systematic benchmarking approach, in which we generate an ensemble of simulated images from the fluctuations of a simulated biopolymer with known mechanical properties. We introduce in these images simulated background noise and other artifacts. In contrast to prior works that have modeled the role of noise on fitting using theoretical assumptions [4], this benchmarking approach provides a rather direct and realistic comparison with actual microscopy data.

### 3.2 *Role of Sampling Error on Estimated Persistence Length*

Here we develop a theory for the error in the estimated biopolymer persistence length $\ell_p$ in terms of the number of sampled images $M$. For this purpose, we assume a biopolymer exhibits fluctuations given by the WLC model, and estimate the covariance

$$\tilde{C}_M = \frac{1}{M} \sum_{m=1}^{M} \mathbf{a}^{(m)} \mathbf{a}^{(m)T}. \tag{16}$$

The $\mathbf{a}^{(m)}$ denotes the $m^{th}$ sample of the modal coefficients. The tilde notation $\tilde{}$ will be used throughout to distinguish variables that model quantities that would be estimated experimentally. The sampling error can be expressed as

$$\tilde{C}_M = C_{wlc}(\ell_p) + \boldsymbol{\xi}. \tag{17}$$

The $C_{wlc}(\ell_p)$ denotes the covariance structure obtained from the WLC model in equation 7. For a sufficient number of samples, we have as a consequence of the Central Limit Theorem that $\boldsymbol{\xi}$ is approximately a Gaussian with mean zero and covariance $\langle \boldsymbol{\xi}\boldsymbol{\xi}^T \rangle = \mathrm{Cov}(\mathbf{a}\mathbf{a}^T)/M$. Expressions for this covariance can be obtained by computing the fourth moments of the Gaussian distribution given in equation 7.

To simplify the presentation, we assume that the components of $[\mathbf{a}]_n$ can be treated as statistically independent. Additionally, we describe our theory only for estimates of the diagonal entries of the covariance matrix, which are the only entries used in the least-squares fitting. In the case of a polynomial basis making $\tilde{S}$ diagonal these assumptions hold and the general case reduces to what we present.

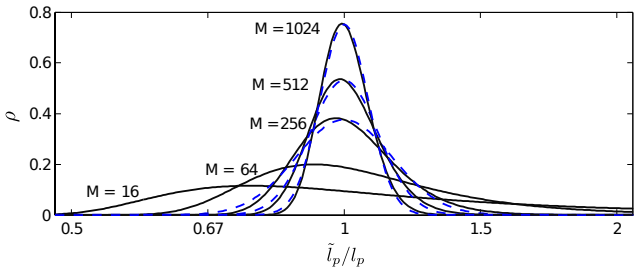


**FIGURE 3 Probability Distribution of Sampling Errors in the Estimate of $\tilde{\ell}_p$ : The sampling error of the estimated non-dimensional persistence length exhibits a non-Gaussian distribution with an infinite second moment. For $M < 100$, the distribution is highly skewed as a consequence of the inverse dependence involving $\ell_p^{-1}$ in the least-squares fit of the estimated biopolymer covariances with sampling errors. However, for $M > 100$, to a good approximation the distribution can be fit with an effective Gaussian distribution. This is shown as the blue dotted curves for $M = 256$, $M = 512$, and $M = 1024$.**

With these assumptions, we denote the diagonal entries of the covariance by the vectors $\tilde{\mathbf{c}}_M = \mathrm{diag}(\tilde{C}_M)$ and $\mathbf{c}_{wlc} = \mathrm{diag}(C_{wlc})$. We model the covariance estimates for $M$ samples by

$$\tilde{\mathbf{c}}_M = \mathbf{c}_{wlc}(\ell_p) + \boldsymbol{\xi}. \tag{18}$$

The $\boldsymbol{\xi}$ denotes a Gaussian with independent components each having mean zero and covariance $\langle \boldsymbol{\xi}\boldsymbol{\xi}^T \rangle = D_M$. The covariance has diagonal entries

$$[D_M]_{n,n} = E[\xi_n^2] = 2[\mathbf{c}_{wlc}(\ell_p)]_n^2/M \tag{19}$$

with the off-diagonal entries zero.

This model can be used to study how sampling errors from the estimate of the modal covariances $\tilde{\mathbf{c}}_M$ propagate into the estimation of the persistence length $\tilde{\ell}_p$. In particular, from the least-squares fit of equation 15, we have

$$\tilde{\ell}_p^{-1} = (\mathbf{d} \cdot \tilde{\mathbf{c}}_M)/\|\mathbf{d}\|^2 = \ell_p^{-1} + \sum_n \xi_n d_n/\|\mathbf{d}\|^2. \tag{20}$$

This shows the estimated inverse persistence length $\tilde{\ell}_p^{-1}$ is a Gaussian-distributed quantity with mean $\tilde{\mu} = \ell_p^{-1}$ and variance $\tilde{\sigma}_M^2 = \mathbf{d}^T D_M \mathbf{d}/\|\mathbf{d}\|^4$.

The estimated persistence length $\tilde{\ell}_p$ has the probability distribution

$$\rho_M(\ell_p) = \frac{\ell_p^{-2}}{\sqrt{2\pi\tilde{\sigma}_M^2}} \exp\left[-\frac{(\ell_p^{-1} - \tilde{\mu})^2}{2\tilde{\sigma}_M^2}\right]. \tag{21}$$

The $\tilde{\mu}$ and $\tilde{\sigma}_M^2$ are defined as above. Note that this distribution is not Gaussian, rather it has long-tails as a consequence of the $\ell_p^{-2}$ term and yields an infinite variance. For different values of $M$ this distribution is shown in Figure 3.

The non-Gaussian form of the distribution requires that some care is taken when characterizing how the sampling errors influence the estimated value of $\tilde{\ell}_p$. We can no longer make use of the standard deviation to give the magnitude of errors since the second moment is infinite. To cope with this issue, we use a confidence interval based on the above probability distribution $\rho_M$. Interestingly, while the second moment is infinite, the distribution $\rho_M$ can be well-approximated by a Gaussian distribution for $M$ sufficiently large ($M > 100$; see Figure 3). Through an asymptotic analysis of equation 21, as $M$ becomes large, we find $\rho_M$ is approximated by a Gaussian with mean $\mu = \ell_p$ and variance $\sigma_M^2 = \ell_p^4 \tilde{\sigma}_M^2 = \ell_p^4 \mathbf{d}^T D_M \mathbf{d}/\|\mathbf{d}\|^4$. This can be used in practice to obtain confidence intervals for errors in estimates of $\tilde{\ell}_p$.

### 3.3 *Generating Simulated Fluorescence Images with Controlled Levels of Noise and Artifacts*

To characterize the quality of proposed spectral analysis methods, we first apply the algorithms to a simulated ensemble of images generated by simulating the fluctuations of a biopolymer with known mechanical properties. We compare how well the methods estimate the known biopolymer mechanical properties when the images are subjected to different levels of noise and artifacts. This provides a well-controlled test for the study of the reliability and accuracy of proposed spectral analysis methods.

To generate noise and artifacts similar to those encountered in experiments, we consider primarily two types of noise, (i) background noise in which randomly varying levels of intensity are seen throughout the image, and (ii) sporadic gaps in which intensity varies in the fluorescence signal along the biopolymer. The background noise is motivated by contributions from ambient light sources and out-of-focus fluorophores in an image. The gap artifacts are motivated by

the uneven binding of fluorescent labels along the biopolymer, inherent fluorescence excitation inefficiencies, and the effects of stochastic photobleaching. Using simulated ensembles of images, we can systematically study how these different sources of noise affect the accuracy of the spectral analysis methods. We then use this information to help optimize experimental conditions and improve measurement precision and accuracy.

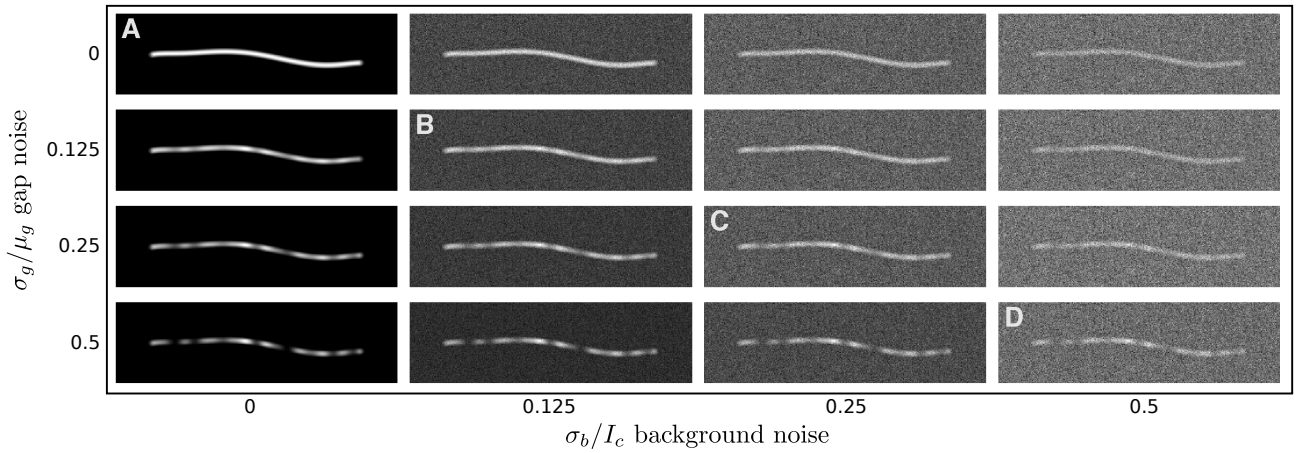


**FIGURE 4 Ensembles of Simulated Fluorescence Images. To investigate our spectral analysis methods when subjected to the types of noise and artifacts found in experimental images, we simulate ensembles of images from a simulated biopolymer with known mechanical properties. Shown here are images generated from biopolymer configurations using our contour representation with $\ell_p = 10$, $N = 8$. The ensembles correspond to different levels of background noise throughout the image and gap artifacts along the biopolymer contour. The background noise increases left to right while the gap artifacts increase from top to bottom. The level of background noise is characterized by the ratio $\sigma_b/I_c$ for the perturbed background pixel standard deviation $\sigma_b$ and the average difference of intensity between the contour and background $I_c$. The level of gap artifacts is characterized by the ratio $\sigma_g/\mu_g$ obtained by integrating the random cosine modulations used to generate the artifacts to obtain an effective mean $\mu_g$ and standard deviation $\sigma_g$.**

To simulate the configurations of a biopolymer having a specified persistence length, we generate modal coefficients for our orthogonal polynomial representation of the contour using the multi-variate Gaussian distribution with mean zero and covariance given by equation 10. Throughout our studies we use $l_p = 10$ and calculate values for the first 8 modes ($N = 8$). To obtain an image with a fluorescence signal for the biopolymer of thickness $r_0$, we use the kernel function of equation 2 to trace along the biopolymer contour. For convenience, we normalize all fluorescence intensity values to lie between zero and one.

To introduce background noise, we perturb each pixel value not on the contour by a Gaussian-distributed random value having mean $\mu_b = 0$ and variance $\sigma_b^2$. Along the contour we perturb pixels with a Gaussian-distributed random value having $\mu_c = 0$ and $\sigma_c^2 = \sigma_b^2$. To characterize the noise, we define $I_c$ to be the characteristic intensity difference between the contour and background $I_c = \langle I(\mathbf{y})\rangle_c - \langle I(\mathbf{y})\rangle_b$, where $\langle\cdot\rangle_\ell, \ell \in \{b, c\}$ gives respectively the average of intensity values over the contour or background pixels. To characterize the level of background noise in our images we use the ratio $\sigma_b/I_c$.

To introduce gap noise along the contour we modulate the fluorescence signal by a weight function obtained from a cosine series $c(s) = \sum_{k=0}^{K-1} w_k \cos(2\pi k s/L)$. The random weight coefficients $w_k$ are chosen so that the integral of $c(s)$ over $[0, L]$ has mean $\mu_g$ and variance proportional to $\sigma_g^2$. The form of $c(s)$ necessitates that $w_0 = \mu_g$. To achieve a variance proportional $\sigma_g^2$, we use $(w_1, ..., w_{K-1})$ uniformly distributed over the surface of a $K-1$ dimensional sphere of radius $\sqrt{2}\sigma_g^2$. To control how oscillatory the gap artifacts appear in the image, we vary the number of modes $K$. We find that $K = 25$ provides a modulation that agrees well with what is seen in experimental fluorescence images. To characterize the level of gap artifacts in our images we use the ratio $\sigma_g/\mu_g$.

### 3.4 *Benchmarking Studies for Different Levels of Noise and Artifitacts*

To investigate the robustness of our methodology, we numerically generate ensembles of fluorescence images with prescribed noise conditions, similar to those observed in experiments. The ensembles contain $M = 1000$ images, simulating the thermal fluctuations of a biopolymer with persistence length $L_p = 9.45L$, where $L$ is the polymer length (taken to be 1 in arbitrary units).

To minimize the effects of sampling errors in these studies, we use the same underlying configurations for the simulated biopolymer to generate each ensemble of images. A sample image from each of these ensembles is shown in Figure 4.

| gap noise | $L_p$ | % err | % conv | $L_p$ | % err | % conv | $L_p$ | % err | % conv | $L_p$ | % err | % conv |
|---|---|---|---|---|---|---|---|---|---|---|---|---|
| 0 | 9.38 | 0.00 | 100 | 9.34 | 0.48 | 100 | 9.37 | 0.10 | 100 | 10.1 | 6.99 | 98 |
| 0.125 | 9.39 | 0.07 | 100 | 9.36 | 0.22 | 100 | 9.42 | 0.43 | 99 | 9.84 | 4.66 | 98 |
| 0.25 | 9.39 | 0.15 | 99 | 9.38 | 0.03 | 99 | 9.45 | 0.77 | 98 | 10.2 | 8.22 | 96 |
| 0.5 | 9.43 | 0.55 | 94 | 9.42 | 0.45 | 94 | 9.71 | 3.35 | 93 | 10.6 | 10.7 | 89 |
| | 0 | | | 0.125 | | | 0.25 | | | 0.5 | | |

background noise

**Table 1 Results for the Simulated Ensembles of Fluorescence Images. To study our spectral analysis methods we simulated ensembles of fluorescence images with varying levels of background noise and gap artifacts generated from the fluctuations of a simulated biopolymer with known persistence length, $L_p = 9.45L$, where $L$ is the polymer length (taken to be 1 in arbitrary units). We report results for our spectral analysis methods using $M = 1000$ simulated images. We report the relative errors (% err) in these estimates and the percentage of images found to be of sufficient quality to allow for convergent fits independent of the initial trial contour (% conv). Relative errors are reported with respect to the baseline case of no background noise or gap artifacts. The table indices correspond to the same ordering and ratios used for characterizing the ensembles of images shown in Figure 4.**

We find that in the absence of any explicitly introduced background noise or gap artifacts our methods yield an estimated non-dimensional persistence length of $\tilde{L}_p = 9.38$. We use this value as our reference when reporting relative errors in order to remove the baseline sampling error from the reported results and better reflect the differences in the levels of noise and artifacts in the images.

For each simulated ensemble of images, we performed the spectral analysis using the initial five Chebyshev modes. We report the results of the spectral analysis using our methods for each of the image ensembles in Table 1.

When performing fits, we find that introduction of noise and gap artifacts can, in a small number of cases, result in images of insufficient quality. For such images (typically less than $5\%$ of the ensemble), the contour fitting does not converge in a manner that is independent of the initial trial contour. These images are ignored when estimating the modal covariances and persistence length. The percentages of images used for each of the reported persistence length values are included in Table 1.

A unique feature of our method is that it globally fits the entire contour to the fluorescence image. The smooth interpolation enables robust determination of persistence length, even in the presence of substantial gap artifacts, which are frequently encountered in experiments. We find relative errors for the estimated persistence length to be $< 1\%$ for a majority of low to moderate noise cases, and $< 10\%$ even for the largest background and gap noise levels probed.

### 3.5 *Experimental Results for Microtubules*

To demonstrate our approach in practice we apply our filament tracing and spectral analysis methods to characterize the persistence length of an isolated microtubule (MT) imaged using total internal reflection fluorescence (TIRF) microscopy. The MT was labeled with rhodamine dyes to enable visualization, confined to move within a thin, well-sealed sample chamber to ensure that the fluctuating filament remained in focus throughout the experiment and only thermal forces acted upon the MT. The experimental details are further described in the Supplemental Materials.

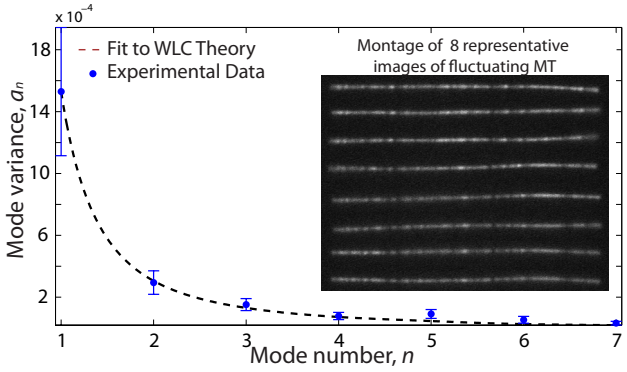


**FIGURE 5 Experimental Results for a Microtubule : We analyse using our spectral analysis methods the thermal fluctuations of a microtubule for $M = 147$ images. The exhibited thermal fluctuations in the microtubule shape are shown in the inset. The exhibited modal covariances of the microtubule fluctuations agree well with a worm-like-chain model (dashed line). The error bars in our analysis correspond to $95.5\%$ confidence intervals using our sampling error analysis in Section 3.2. Our methods yield an actual dimensional persistence length of $\tilde{L}_p = 3.45 \pm 0.52$ mm.**

As a test of our approach, an ensemble of $M = 147$ fluorescence microscopy images were obtained and analyzed using our contour fitting method and least-squares estimator to analyze the first four modes. From these, we determine a non-dimensional persistence length of $\tilde{\ell}_p = 176.6$ using the spectral characteristics of the fluctuating filament, see Figure 5. In this test case, the microtubule contour length was estimated to be $\tilde{L} = 19.6\mu$m. This gives an actual dimensional persistence length of $\tilde{L}_p = 3.45$mm. To determine the uncertainty in this measurement, we consider errors arising from both sampling and image artifacts. We estimate the sampling error when using only $M = 147$ images to be $\pm.48$mm in $\tilde{L}_p$. From analysis of the experimental fluorescence images, we estimate an average effective background noise of $\sigma_b/I_c = 0.143$ and average effective gap noise of $\sigma_g/\mu_g = 0.184$. From the results of a benchmarking study performed under similar noise conditions, we estimate the contribution to $\tilde{L}_p$-uncertainty of $\pm 0.2$mm. We anticipate that the uncertainties due to sampling errors and

noise artifacts behave in a fairly independent manner. Under this assumption, the total uncertainty can be estimated by adding these two contributions in quadrature. Therefore, we estimate $\tilde{L}_p = 3.45 \pm 0.52$ mm. These results represent a measurement uncertainty of $\approx 15\%$. Our measured persistence length is well-within the range of previously reported values [29, 30]. The dashed black line in Figure 5 shows the variances for the Chebyshev modes predicted using a WLC model with the same mean bending stiffness. We find good agreement between the WLC model and our spectral data, validating our fitting algorithm under experimental conditions and relatively small sample sizes. Moreover, we find good agreement with the WLC prediction for at least six independent modes.

## 4. SUMMARY

New spectral analysis methods were presented for the measurement of biopolymer flexural rigidity from observations of the biopolymer thermal fluctuations. Our approach was based on global fitting of an entire trial contour at once to the fluorescence image. We used a contour representation expressed in terms of a curve parameterized by arc-length with specified tangent angles expanded in a basis of orthogonal polynomials. Using this representation we performed statistical analysis of the modal coefficients to infer a flexural rigidity for the biopolymer.

To investigate the robustness and accuracy of spectral analysis methods, we developed a benchmarking approach based on a simulated ensemble of images with realistic noise artifacts generated from the configurations of a simulated fluctuating biopolymer with known mechanical properties. Our spectral analysis methods were found to work very well even in the case of images exhibiting significant background noise and gap artifacts. In contrast to contour tracing approaches that make use of primarily local information, our new more global methods allow for robust fits that interpolate and filter information in the fluorescence image providing tolerance to sporadic gaps in the fluorescent intensity along the biopolymer and other types of noise. The benchmarking approach we propose provides a potentially powerful metric for rating different spectral analysis methods and for understanding the statistical significance of differences reported in experimental results.

To demonstrate our methods in practice, we studied experimental fluorescence images of a fluctuating microtubule. We found good agreement in the covariance structure of the modes of the fitted contours with the worm-like chain model for at least six different modes and measurement uncertainties of $\approx 15\%$. These results were obtained for a relatively small sample of images, $M = 147$, showing the promise of our approach.

Our results indicate that these new spectral analysis methods provide a substantial improvement in precision for measurements of stiffness based on observed fluctuations of a biopolymer. We expect these approaches will enable future studies of the differential effects of polymerization conditions and MAPs on microtuble mechanics.

## 5. ACKNOWLEDGEMENTS

Authors thank Professor Leslie Wilson (UCSB) for providing tubulin proteins and Anna Simon for useful discussions, and gratefully acknowledge support from the National Science Foundation (CAREER Award 0956210 to PJA and IGERT DGE-0221715 for DV), a Burroughs Wellcome Fund Career Award at the Scientific Interface (to MTV), and a research award from CurePSP (MTV and DY).

## REFERENCES

1. D.A. Fletcher and R.D. Mullins. Cell mechanics and the cytoskeleton. *Nature*, 463(7280):485–492, 2010.
2. H. Felgner, R. Frank, J. Biernat, E.M. Mandelkow, E. Mandelkow, B. Ludin, A. Matus, and M. Schliwa. Domains of neuronal microtubule-associated proteins and flexural rigidity of microtubules. *The Journal of cell biology*, 138(5):1067, 1997.
3. H. Felgner, R. Frank, and M. Schliwa. Flexural rigidity of microtubules measured with the use of optical tweezers. *Journal of cell science*, 109:509, 1996.
4. F. Gittes, B. Mickey, J. Nettleton, and J. Howard. Flexural rigidity of microtubules and actin filaments measured from thermal fluctuations in shape. *The Journal of cell biology*, 120(4):923, 1993.
5. M.E. Janson and M. Dogterom. A bending mode analysis for growing microtubules: evidence for a velocity-dependent rigidity. *Biophysical journal*, 87(4):2723–2736, 2004.
6. B. Mickey and J. Howard. Rigidity of microtubules is increased by stabilizing agents. *The Journal of cell biology*, 130(4):909, 1995.
7. J. van Mameren, K.C. Vermeulen, F. Gittes, and C.F. Schmidt. Leveraging Single Protein Polymers To Measure Flexural Rigidity. *The Journal of Physical Chemistry B*, 113(12):3837–3844, 2009.
8. G. Cooper. Cytoskeletal networks and the regulation of cardiac contractility: microtubules, hypertrophy, and cardiac dysfunction. *Am. J. Physiol. Heart Circ. Physiol.*, 291:H1003–H1014, 2006.
9. D.R. Webster. Microtubules in cardiac toxicity and disease. *Cardiovascular Toxicology*, 2(2):75–89, 2002.
10. G.A. Buxton, S.L Siedlak, G. Perry, and Smith M.A. Mathematical modeling of microtubule dynamics: Insights into physiology and disease. *Progress in neurobiology*, 92:478–483, 2010.
11. F. Lautenschläger, S. Paschke, S. Schinkinger, A. Bruel, M. Beil, and J. Guck. The regulatory role of cell mechanics for migration of differtiating myeloid cells. *PNAS*, 106(37):15696–15701, 2009.
12. P.J. Keller, Pampaloni. F., G. Lattanzi, and E.H.K. Stelzer. Three-dimensional microtubule behavior in Xenopus egg extracts reveals four dynamic states and state-dependent elastic properties. *Biophysical Journal*, 95(3):1474–1486, 2008.
13. E. Nogales, S.G. Wolf, I.A. Khan, R.F. Ludueña, and K.H. Downing. Structure of tubulin at 6.5 Å and location of the taxol-binding site. *Nature*, 391:199–203, 1995.
14. E. Nogales, M. Whittaker, R.A. Milligan, and K.H. Downing. High-resolution model of the microtubule. *Cell*, 96(1):79–88, 1999.
15. E. Nogales, S.G. Wolf, and K.H. Downing. Structure of the tubulin dimer by electron crystallography. *NATURE-LONDON-*, 391:199–202, 1998.
16. H.W. Wang and E. Nogales. Nucleotide-dependent bending flexibility of tubulin regulates microtubule assembly. *Nature*, 435(7044):911–915,

2005.

17. M. Kikkawa, T. Ishikawa, T. Nakata, T. Wakabayashi, and N. Hirokawa. Direct visualization of the microtubule lattice seam both in vitro and in vivo. *The Journal of cell biology*, 127(6):1965, 1994.
18. K.J. B
"ohm, W. Vater, H. Fenske, and E. Unger. Effect of microtubule-associated proteins on the protofilament number of microtubules assembled in vitro. *Biochimica et Biophysica Acta (BBA)-General Subjects*, 800(2):119–126, 1984.
19. D. Chretien, F. Metoz, F. Verde, E. Karsenti, and RH Wade. Lattice defects in microtubules: protofilament numbers vary within individual microtubules. *The Journal of cell biology*, 117(5):1031, 1992.
20. G.B. Pierson, P.R. Burton, and R.H. Himes. Alterations in number of protofilaments in microtubules assembled in vitro. *The Journal of cell biology*, 76(1):223, 1978.
21. F. Pampaloni, G. Lattanzi, A. Jonáš, T. Surrey, E. Frey, and E.L. Florin. Thermal fluctuations of grafted microtubules provide evidence of a length-dependent persistence length. *Proceedings of the National Academy of Sciences*, 103(27):10248, 2006.
22. MGL van den Heuvel, S. Bolhuis, and C. Dekker. Persistence length measurements from stochastic single-microtubule trajectories. *Nano letters*, 7(10):3138–3144, 2007.
23. MGL Van den Heuvel, MP de Graaff, and C. Dekker. Microtubule curvatures under perpendicular electric forces reveal a low persistence length. *Proceedings of the National Academy of Sciences*, 105(23):7941, 2008.
24. P.W. Bass and L. Qiang. Neuronal microtubules: when the MAP is the roadblock. *Trends in cell biology*, 15(4):183–187, 2005.
25. G. Morfini, G. Pigino, Beffert U., Busciglio J., and Brady S.T. Fast axonal transport misregulation and Alzheimer's disease. *NeuroMolecular Medicine*, 2:89–99, 2002.
26. K. Iqbal, F. Liu, C.X. Gong, A. del C. Alonso, and I. Grundke-Iqbal. Mechanisms of tau-induced neurodegeneration. *Acta Neuropathology*, 118:53–69, 2009.
27. C.P. Brangwynne, G.H. Koenderink, E. Barry, Z. Dogic, F.C. MacKintosh, and D.A. Weitz. Bending dynamics of fluctuating biopolymers probed by automated high-resolution filament tracking. *Biophysical journal*, 93(1):346–359, 2007.
28. L.N. Trefethen. *Spectral methods in MATLAB*. Society for Industrial Mathematics, 2000.
29. J. van Mameren, K.C. Vermeulen, F. Gittes, and C.F. Schmidt. Leveraging single protein polymers to measure flexural rigidity. *J. Phys. Chem. B*, 113:3837–3844, 2009.
30. M. Kikomoto, M. Kurachi, V. Tosa, and Tashiro H. Flexural rigidity of individual microtubules measured by a buckling force with optical traps. *Biophysical Journal*, 90:1687–1696, 2006.
31. C.S. Peskin. The immersed boundary method. *Acta Numerica*, 11:479–517, 2002 2002.
32. Paul J. Atzberger, Peter R. Kramer, and Charles S. Peskin. A stochastic immersed boundary method for fluid-structure dynamics at microscopic length scales. *J. Comp. Phys.*, 224(2):1255–1292, JUN 10 2007.
33. I. M. Gelfand and S. V. Fomin. *Calculus of Variations*. Dover, 2000.
34. N. Saitô, K. Takahashi, and Y. Yunoki. The statistical mechanical theory of stiff chains. *J. Phys. Soc. Jpn*, 22:219–225, 1967.
35. L. E. Reichl. *A Modern Course in Statistical Physics*. Jon Wiley and Sons Inc., 1997.